Two-Color Thermography of GMAW to Enable Real-Time Hardness Prediction

A commercial color camera measured melt pool temperatures using real time images to qualify mechanical properties typically evaluated post processing

BY G. C. SOLIS, A. J. MYERS, G. QUIRARTE, B. MONDAL, J. A. MALEN, AND S. P. NARRA

Abstract

Advanced process monitoring and model validation are essential for improving weld quality in both welding and welding-based additive manufacturing processes. Specifically, temperature is a key quantity of interest for understanding defect formation and microstructural evolution, which significantly impact mechanical properties. However, achieving accurate in-situ temperature imaging is challenging due to emissivity variations across the dynamic melt pool. To address this, we implemented a two-color imaging technique using a single commercial color camera to reduce temperature readings' sensitivity to emissivity variations. High dynamic range images during melting were captured at various exposure times, and spatial and temporal filters were applied to minimize interference from the plasma arc emissions. The resulting temperature fields within the melt pool were then utilized to estimate cooling rates, which were further correlated to ex-situ hardness measurements. The strong correlation observed between cooling rates ranging from 20 to 600 K/s and hardness ranging between 250 to 400 HV demonstrated the potential of our easy-to-use two-color thermal imaging setup for preliminary evaluation of mechanical properties in a non-destructive manner. Beyond its significance for predicting mechanical properties, this technique provides a validated temperature measurement approach that can enhance the accuracy of physics-based models, such as those used to predict defect formation mechanisms, like porosity.

https://doi.org/10.29391/2025.104.027

Keywords

- Gas Metal Arc Welding (GMAW)
- Melt Pool Temperature
- Two-Color Thermography
- In-Situ Monitoring
- Property Prediction

Introduction

Welding process monitoring tools have been developed to enhance component quality and support certification across different industrial applications (Refs. 1–3). Typical methods include signal input sensors that monitor electrical parameters, like current and voltage, arc measurements that gauge arc length and stability, and thermal sensing techniques such as infrared (IR) thermography and pyrometry, which track thermal emission and spatially averaged temperature (Refs. 4, 5). Welding-based processes, including weld repair, joining, and additive manufacturing, encounter common challenges related to controlling microstructural variability, including defects, primarily caused by changes in thermal conditions. These processes typically use a heat source and consumable wire feedstock to create joints and complex structures that pose varied heat dissipation pathways for cooling. Such thermal variability can cause non-uniform microstructures across the weld, impacting part geometry and mechanical properties (Refs. 6–9).

Building on these challenges, extensive research has highlighted the significant influence of solidification conditions on microstructural features such as grain size and phase distribution (Refs. 5, 10, 11). Solidification conditions, which vary based on factors like position within the base plate, alloy composition, and heat input parameters, are crucial for controlling the microstructure, affecting mechanical properties such as hardness, toughness, and fatigue resistance (Refs. 12, 13). Recent advances, such as the photodiode-based

Table 1 — Elemental Composition (wt-%)

		C	Cr	Mn	Mo	Ni	P	S	Si	V	Cu
SuperArc L-59	Min.	0.07	0.02	1.42	–	0.01	0.005	0.017	0.81	–	0.12
	Max.	0.1	0.05	1.49	0.01	0.02	0.01	0.027	0.89	0.005	1.23
A36-HRPO Steel	Min.	0.25	–	0.6	–	–	–	–	–	–	0.2
	Max.	0.29	–	0.9	–	–	0.04	0.04	0.5	–	–

Planck thermometry introduced by Jeong et al., enable the measurement of rapid cooling rates exceeding 5000 K/s, which surpasses traditional IR-based methods (Ref. 14). This highlights the feasibility of collecting precise real-time thermal data to better understand and control solidification processes and resulting microstructures (Ref. 15). Researchers such as Xie et al. have demonstrated how real-time data collection methods can be utilized to control cooling rates more precisely, thereby enhancing the predictability and uniformity of microstructural outcomes (Ref. 16). Following this approach, non-contact thermal monitoring technologies have been advocated to inform manufacturers on how to dynamically adjust processing parameters. Such adjustments seek to achieve uniform cooling across the build, leading to more consistent material properties throughout the part (Ref. 10). This strategy of real-time monitoring and adjustment, central to modern manufacturing paradigms, highlights the evolving capabilities in capturing the dynamic behavior of the moving melt pool and using these insights to optimize component quality.

Thermal imaging is the ideal process monitoring technique to detect changes in local thermal behavior that cause inconsistent solidification, undesired microstructures, and inhomogeneous properties (Refs. 17, 18). Contact thermal measurement techniques, such as thermocouples, face challenges in measuring dynamic thermal fields because they are placed in a single location distant from the melt pool, and the probe itself could alter the thermal distribution being measured (Ref. 7). Non-contact techniques such as IR and monochromatic visible imaging infer temperature by assuming a constant and uniform emissivity (Refs. 19–21). However, a material's emissivity is a function of temperature and wavelength, making it difficult to accurately measure the temperature within a dynamic melt pool (Ref. 22). To address the limitations of current thermal monitoring methods, a ratiometric optical pyrometer system using two separate cameras was utilized to measure melt pool temperatures in wire-based additive manufacturing processes. By capturing the ratio of radiation emissions from select wavelength bands using two separate cameras, the temperature measurements become insensitive to emissivity and can correlate thermal data with geometrical changes (Refs. 22–25). While effective at capturing thermal distributions in a dynamic melt pool, this approach involves a complex setup requiring synchronization of two separate monochromatic cameras, various optical components, intricate alignment, and extensive calibration.

Table 2 — CMOS Camera Specifications

Camera Model	BFLY-PoE-2326C-C
Pixel Size, H × W (μm)	5.86 × 5.86
Frame Size (pixels)	1920 × 1200
Max Frame Rate (fps)	21 max. at highest resolution
Bit Depth (bit)	16

Methods that utilize an optical camera have been developed for thermal imaging. One method splits the image into two projections that pass through different filters and are incident on separate halves of the same monochromatic detector (Ref. 26). The two images are aligned in post processing, and ratiometric temperatures are computed. Vallabh et al. implemented this approach to image Inconel 718 in the laser powder bed fusion of process, enabling the prediction of melt pool depth and grain size using temperature gradients (Ref. 27). Their study highlights the potential to predict essential microstructural characteristics in real-time using in-situ temperature monitoring. A recent simplification employed visible-range color cameras that reported three separate color values at each pixel, enabling ratiometric temperature measurements without additional optical equipment. With a high-speed color camera, Myers and Quirarte et al. accurately measured melt pool temperatures for laser powder bed fusion process. The thermal images were used for calibration of a computational fluid dynamics model and extended to other additive manufacturing processes to demonstrate the use of commercial color cameras for accurate thermal imaging of melt pools (Refs. 28–30). Given the links between microstructure and properties, temperature monitoring with a color camera promises prediction and qualification of critical mechanical properties without requiring destructive evaluation, at a minimum for preliminary assessment.

In this study, the two-color method using a single commercial color camera was used to measure melt pool temperatures using real time images, aiming to qualify mechanical properties that are typically evaluated post processing in welding-based processing. While two-color

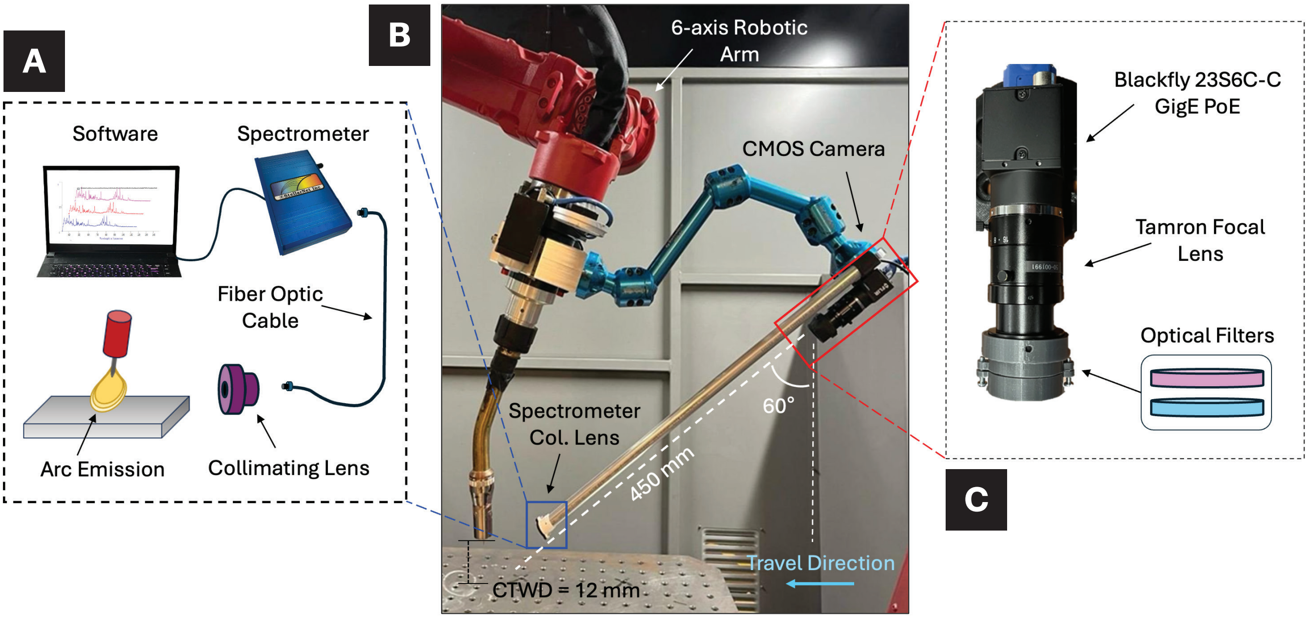

Fig. 1 — A — StellarNet spectrometer setup schematic; B — welding gun with spectrometer attached via fiber optic cable mounted (aluminum rod) on Blackfly's swivel arm mount. The swivel is attached to the upper part of the welding gun with a CNC machined aluminum block to be used as a stable bracket; C — FLIR Blackfly 23S6C color camera, focal lens, and filters.

imaging is an established approach, we show that applying it to arc-based welding has unique challenges related to the impact of plasma arc interference on the accuracy of temperature measurements. This research aimed to answer the following questions: (1) How does the two-color method handle optical interference from the plasma arc during temperature measurement of the melt pool? (2) Can the thermal data obtained be correlated with variations in cooling rates and subsequent mechanical properties?

Experimental Procedures

Material Deposition Experiments with Monitoring Setup

A total of 108 single-track experiments were conducted for thermal imaging using a Lincoln Electric wire arc additive manufacturing (WAAM) cell. This setup consisted of a gas metal arc welding (GMAW) gun mounted on a six-axis ABB robotic arm and a two-axis positioning bed, as shown in Fig. 1. Each 100 mm single-track was deposited with a minimum 25 mm separation from the previous bead with a minimum of 10-min hold time to prevent significant heat accumulation between tracks. Deposition was performed using SuperArc® L-59®, a 1.2-mm-diameter copper-coated low-carbon steel wire, on 1-in.-thick A36-HRPO steel base plates. The process was carried out under a shielding gas mixture of 85% CO_2 and 15% Ar. The compositions of both the filler wire and baseplate are detailed in Table 1 (Refs. 31, 32).

In welding, the metal transfer mode contributes to the heat input and the formation of the molten droplet (Ref. 33). The metal transfer mode used in this study was Surface Tension Transfer® (STT), a proprietary Lincoln Electric variant of the short-circuit (SC) transfer mode known for stability and control (Ref. 34). In conventional SC transfer, the current drawn from the power supply is directly dependent on the wire feed speed (WFS). STT, however, modulates the current waveform in real time, allowing for independent control of peak, background, and pinch currents. This minimizes spatter and reduces heat input by precisely managing the detachment of molten metal droplet (Ref. 35). A qualitative comparison of STT and SC waveforms is shown in Appendix A, Fig. A.12.

To evaluate the effects of processing conditions, WFS values of 45 mm/s, 56.5 mm/s, 67.7 mm/s, and 80 mm/s were examined with travel speeds (TS) of 5 mm/s, 12 mm/s, and 20 mm/s. Since STT dynamically modulates current and voltage in real time, the input power does not remain constant but fluctuates throughout the deposition. However, when measured power was averaged over the duration of each track, it exhibited a linear relationship with WFS, as shown in Appendix A, Fig. A.13.

A FLIR Blackfly 23S6C-C PoE GigE machine vision color camera was mounted on a swivel arm near the welding gun, secured with a customized aluminum bracket to ensure stability during processing. Table 2 details the camera's specifications (Ref. 36). Due to the positioning of the welding gun, the orthogonal view of the melt pool was inaccessible, as the gun obstructed the direct overhead camera placement. Figure 1 illustrates the distance between the welding gun and the CMOS camera. A Tamron M112FM50 1/1.2-in. focal lens (Ref. 37), with an aperture range of f/2.8 to f/16 and a 50 mm focal length, was attached to the Blackfly camera's C-mount. To correct distortions related to the camera's angled perspective and ensure an accurate dimensional representation of the melt pool, a homography matrix was

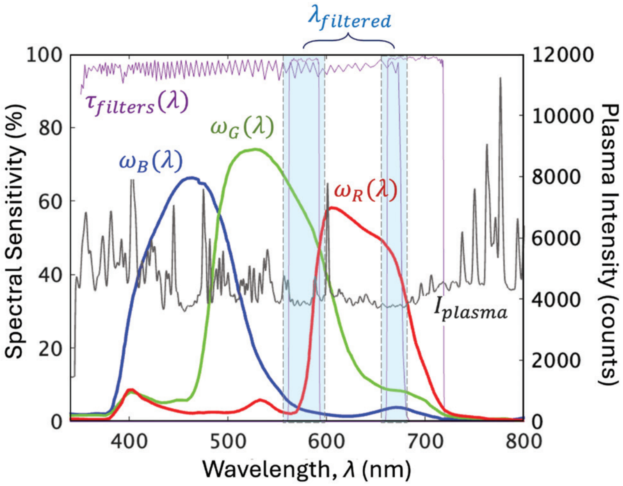

Fig. 2 — Spectral sensitivity of the camera's red ($\omega_R(\lambda)$), green ($\omega_G(\lambda)$), and blue ($\omega_B(\lambda)$) channels. The plasma intensity (I_{plasma}) is superimposed to show the wavelengths of the higher spectral intensity bands that affect the sensor's sensitivity. The highlighted wavelength bands ($\lambda_{filtered}$) represent the ranges of remaining wavelengths after applying the selected bandpass filters ($\tau_{filters}(\lambda)$).

applied to the captured images (Ref. 29). This geometric correction aligned the pixel coordinates to a plane orthogonal to the optical axis, standardizing measurement and analysis across all image frames (see Appendix A.4, Fig. A.15).

One of the unique challenges associated with monitoring arc-based welding processes is optical interference from the plasma arc (Ref. 38). The plasma arc emits high-intensity light across a broad range of wavelengths, interfering with the visible spectrum of the camera. This interference causes pixel saturation in frames captured during arcing periods, leading to inconsistent and unreliable temperature measurements. Although successful images can be taken without filters, to improve the signal-to-noise ratio and align the captured wavelengths with the lower-intensity regions of the arc emission spectrum, optical filters were applied to block the high-intensity plasma.

Before selecting the appropriate filters, the plasma's spectral emission was characterized using a StellarNet BW-VIS spectrometer with a spectral range of 350–1150 nm and a spectral resolution of 1 nm with a 25 µm slit. The spectrometer was connected via a 2-m fiber optic cable and a collimating lens and positioned inside the welding cell near the gun, as shown in Fig. 1. Spectral intensity measurements were recorded every 50 ms during a 100 mm bead experiment at a TS of 5 mm/s. Figure 2 presents the measured plasma intensity curve over the visible wavelength range, overlaid with the spectral sensitivity of the camera's CMOS Bayer pattern sensor.

To effectively minimize plasma interference, a short-bandpass filter with a cutoff at 750 nm and a dual-bandpass filter with transmission bands centered at 577 nm and 690 nm were selected. These two filters were mounted onto the focal lens using a custom-designed, 3D-printed adapter. Their transmission responses, shown in purple ($\tau_{filters}$) in Fig. 2, illustrate the selective suppression of plasma intensity peaks. The wavelengths remaining after filtering are shaded in blue ($\lambda_{filtered}$). With these filters installed, the usable spectral bands were restricted to 577 ± 17 nm and 670 ± 10 nm, corresponding to the red ($\lambda_{filtered,R}$) and green ($\lambda_{filtered,G}$) channels of the camera sensor. This filtering approach enhanced the accuracy of thermal imaging by improving signal-to-noise ratio.

Two-Color Imaging Technique

The two-color approach is based on Planck's Law, expressed in Eq. 1, which governs the intensity of electromagnetic radiation emitted from a blackbody ($L_{\lambda,b}$) as a function of wavelength (λ) and temperature (T). The constants used in the equation are $c_1 = 1.191 \cdot 10^{-4}\ \mu m^2/sr$ and $c_2 = 1.439 \cdot 10^4\ \mu mK$.

$$L_{\lambda,b}(\lambda,T) = \frac{C_1}{\lambda^5\left[exp\left(\frac{C_2}{\lambda T}\right)-1\right]} \tag{1}$$

The CMOS camera sensor integrates the light incident on each pixel over the exposure time (Δt). In the case of an RGB camera, the CMOS sensor is covered by a Bayer filter array consisting of three distinct color filters, red, green, and blue, to enable color imaging within the visible spectrum. The spectral sensitivity for the red, green, and blue channels of the FLIR Blackfly ($w_{i,R}(\lambda)$, $w_{i,G}(\lambda)$, $w_{i,B}(\lambda)$) are shown in Fig. 2. The signal (S_i) is defined as,

$$\begin{aligned} &S_i(T_i,\Delta t) \\ &= C_i\Delta t \int w(\lambda)\tau(\lambda)\epsilon_i(\lambda,T_i)L_{\lambda,b}(T_i)d\lambda \end{aligned} \tag{2}$$

where light incident on a pixel i is represented by the integrand of Equation 2, and $L_{\lambda,b}(T_i)$ is multiplied by the channel's spectral sensitivity ($w(\lambda)$), any additional filter or optical losses ($\tau(\lambda)$), and the material's emissivity ($\epsilon_i(\lambda,T_i)$. This product is then integrated between a band of wavelengths and multiplied by the camera's Δt and constant of proportionality (C_i) to determine S_i (Ref. 28). Typical steels have emissivity variations of less than 5% across the red and green channel spectral bands at room temperature. Hence, the emissivity of a grey body is assumed to be independent of wavelength and only as a function of temperature (Ref. 39). This assumption enables the use of the red-to-green channel ratio, $r_{R/G}$, to define a quantity that remains insensitive to emissivity,

$$\begin{aligned} r_{R/G}(\lambda,T) &= \frac{S_{i,R}(T_i\,,\Delta t)}{S_{i,G}(T_i\,,\Delta t)} \\ &= C_{R/G}\frac{\int w_R(\lambda)\tau(\lambda)L_{\lambda,b}(T_i)d\lambda}{\int w_G(\lambda)\tau(\lambda)L_{\lambda,b}(T_i)d\lambda} \end{aligned} \tag{3}$$

In this ratiometric equation, the only unknown is the calibration constant of proportionality, $C_{R/G}$, which is determined through measurements of a calibrated reference used during the validation phase.

Temperature Validation

The accuracy of the two-color temperature measurements was validated by capturing images of a tungsten filament lamp (S8.5-200 Pyrometer LLC) at different temperatures using the Blackfly color camera. The electrical currents necessary for the tungsten filament to reach specified temperatures were calibrated and compared to NIST standards by Pyrometer LLC. For temperature measurement validation, the images were taken with the same set of filters that were chosen for minimizing arc interference and for the same Δt used for imaging weld beads. The experimental setup is described in detail in Appendix A.2.

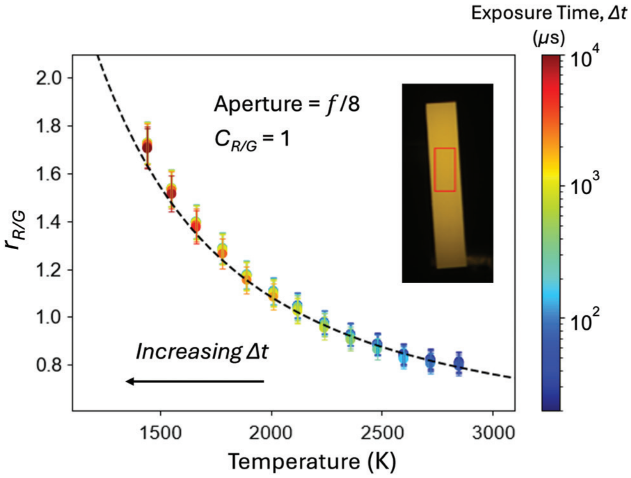

Fig. 3 — Camera signal validation curve comparing the experimental red-to-green channel ($r_{R/G}$) intensity ratio as a function of temperature to the theoretical curve.

The experimentally measured signal ratios from the two-color system were compared to theoretical temperature predictions calculated using Eq. 3, accounting for the spectral characteristics of the new filters through $\tau(\lambda)$. As seen in Fig. 3, there is an excellent agreement between the experimental data and the theoretical prediction of $r_{R/G}$, with $C_{R/G} = 1$.

Image Processing and Data Preparation

The average pixel intensity at a single Δt across individual frames from a single-track experiment is shown in Fig. 4A, where high-intensity peaks correspond to the arcing period and lower intensities represent the short-circuit period. This differentiation is important for identifying frames that can be reliably used for thermal imaging. Figure 4B shows the conversion from optical to thermal images during these different stages, demonstrating the effect of pixel saturation from the plasma arc during the arcing period. Due to these significant intensity fluctuations observed during these phases, a threshold (red dashed line in Fig. 4A) was applied to filter the frames with high-intensity peaks causing saturation in the thermal images. Frames exceeding this threshold were excluded from the dataset, minimizing the effects of the plasma arc on the melt pool temperature measurements. The remaining frames after applying the selected threshold value were averaged to create a single melt pool image, from which centerline temperature profiles were captured.

A range of apertures and Δt were tested to reduce the need for manual lens adjustments after each experiment while also allowing for visualization of different areas of the melt pool. From Fig. 4C, it is clear that saturated regions of the melt pool

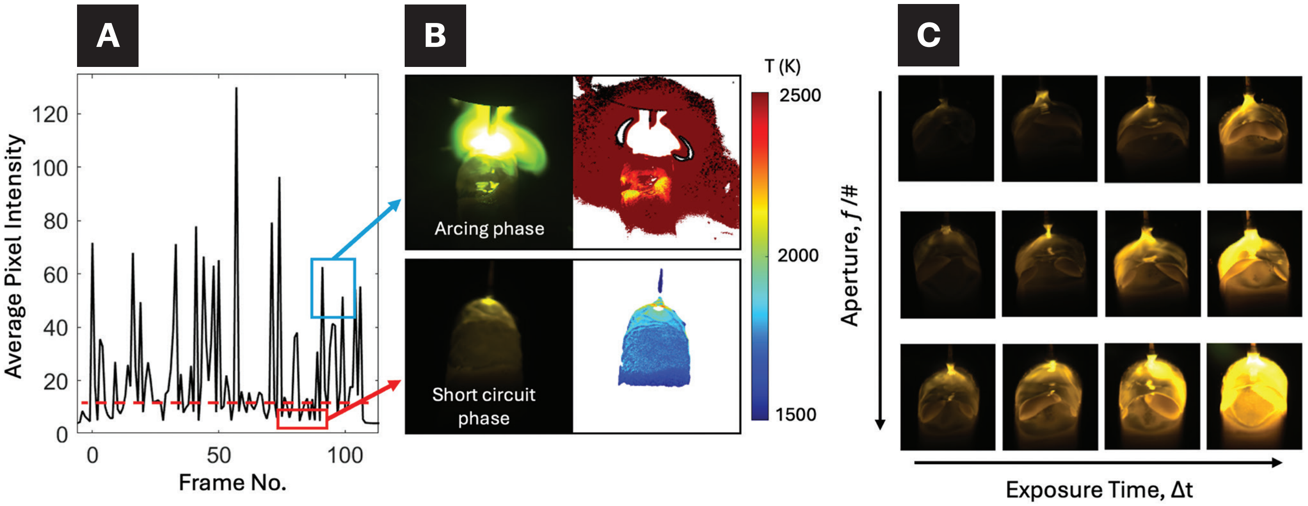

Fig. 4 — A — Average pixel intensity per frame in a single-track experiment, taken at Δt = 1200 μs; B — the top image shows the optical and thermal image of the melt pool during the arcing period. The high intensity of the plasma arc causes saturation in the image, even at lower Δt. *The lower image shows a frame during the short-circuit period with no evidence of saturation; C — melt pool images taken at varying apertures and* Δt *to find optimal camera parameters.*

were reduced by decreasing Δt and numerical aperture (Ref. 40). A constant aperture of f/8 was selected, paired with three Δt: 50 μs, 350 μs, and 1200 μs to minimize saturation and maximize melt pool coverage. Figure 5 shows the temperature conversions of the averaged melt pool frames for the same processing parameters at different Δt. To capture steady-state melt pool geometry, only frames corresponding to the middle portion, between 20 mm and 80 mm, were used for averaging.

Cooling Rate Estimation from In-Situ Thermography

A composite image was formed from all the average frames to create a comprehensive temperature distribution of the melt pool, as shown in Fig. 6A. The composite thermal images were used to quantify the molten pool cooling rate, estimated by the product of the centerline temperature gradient (*dT/dx*) and the TS. While cooling rates are typically measured at the tail of the melt pool, between the liquidus and solidus temperatures, we instead chose to measure cooling rates in the molten region of the melt pool (e.g., in Fig. 6B, this region is identified by ΔT), primarily to reduce measurement uncertainty. This is referred to as the measured molten pool cooling rate. Error bars for cooling rates were obtained by calculating the standard deviation from multiple measurements taken from consecutive thermal images at the same processing conditions.

Using a conduction-based moving heat source model, prior work by Tang et al. (Ref. 41) shows that the cooling rate between two points along the centerline of the melt pool is proportional to the thermal conductivity of the material, TS,

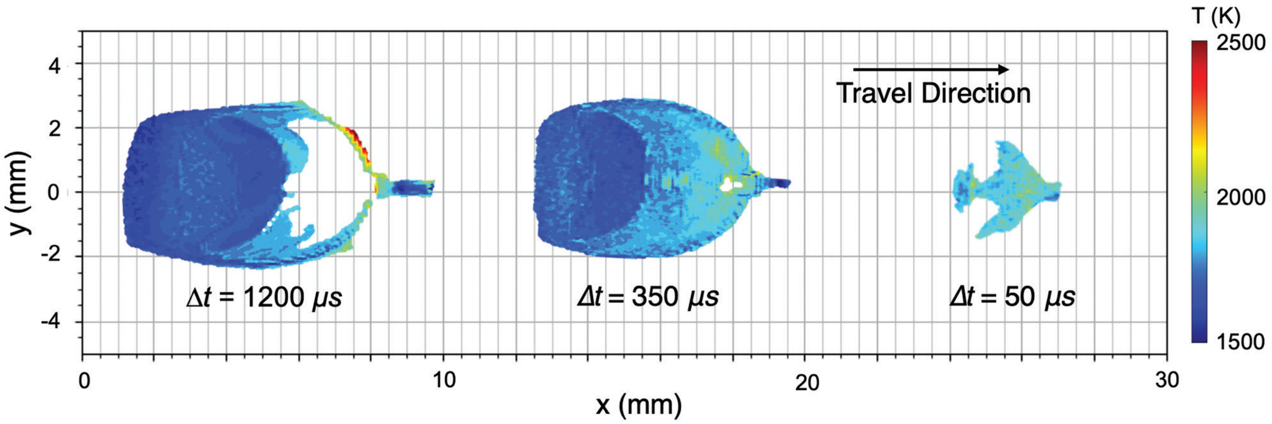

Fig. 5 — Thermal images using $r_{R/G}$ of the melt pool captured at Δt = 1200, 350, and 50 μs during a single-track experiment using constant processing parameters (TS = 5 mm/s, WFS = 67.7 mm/s).

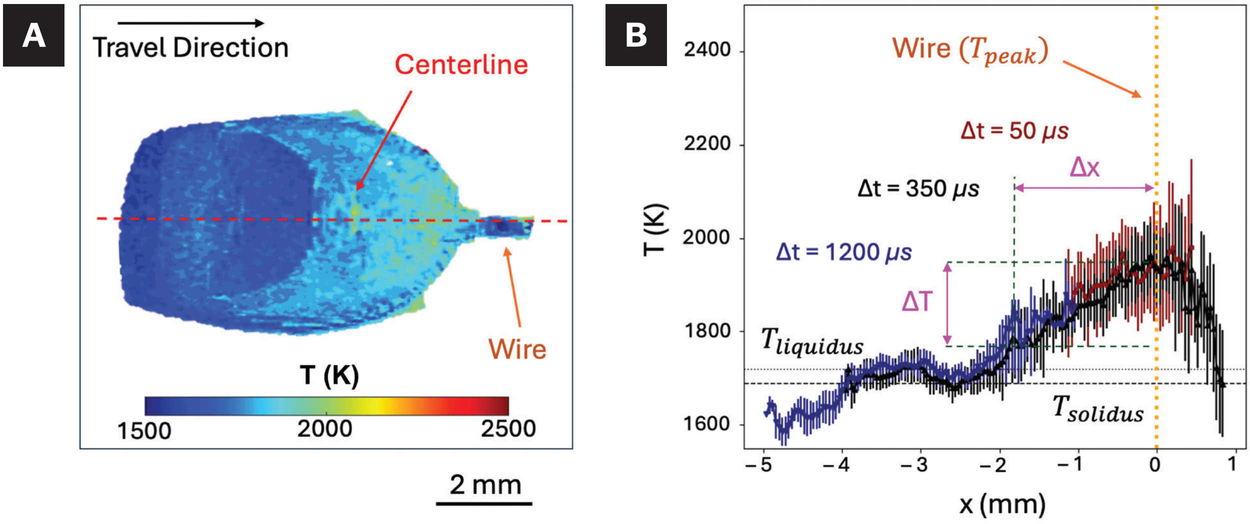

Fig. 6 — A — Composite thermal image of a melt pool, derived from averaged frames at Δt = 50, 350, and 1200 μs during single-track experiment using constant process parameters (TS = 5 mm/s, WFS = 67.6 mm/s); B — the centerline temperature profile is analyzed using 80 frames taken from the 20 to 80 mm portion of the single-melt track. Noise near the electrode region suggests potential interferences from arc reflections, melt pool plume, and lens artifacts.

and input power for a given preheat/background temperature. This means cooling rates calculated from two sets of temperatures along the centerline will scale proportionately when conduction is the only heat transfer mode. However, this scaling may not be proportional between the cooling rate within the melt pool and the cooling rate within the solid. This is because within the melt pool, heat transfer is influenced by phenomena other than conduction, such as convection and radiation. Hence, while the qualitative variations in the measured molten pool cooling rate as a function of WFS and TS are representative of the variations at a lower temperature range, the quantitative scaling between the two requires further investigation.

Microstructure Characterization and Hardness Testing

After printing multiple single tracks for each processing parameter set imaged with multiple Δt, the base plates with bulk samples were sectioned at the center of the plate to reveal the y-z cross-section (positive x direction being the travel direction) using an abrasive saw The sectioned samples were compression-mounted using Buehler KonductoMet conductive powder, then ground with 120 to 320 grit SiC until flat. Using the Buehler auto-polishing system, the plane samples were polished with the CarbiMet surface and 9 µm MetaDi Supreme Diamond abrasive, followed by the UltraPad surface with 3 µm MetaDi abrasive, and finished with the ChemoMet surface and 0.05 µm MasterPrep Alumina abrasive, as suggested by the Buehler handbook (Ref. 42).

Polished samples were etched using a Nital solution to reveal the microstructural details, specifically the fusion zone boundary, which is the interface between the melted and solidified material and the surrounding unaffected base material. Following ASTM E407-07, *Standard Practice for Microetching Metals and Alloys,* the Nital mixture contained 3 mL of nitric acid (HNO_3) and 100 mL of methanol (95%) (Ref. 43). Each sample was submerged in the solution for 30 s, allowing sufficient contrast for microstructural examination without over-etching. Following the etching process, the samples were examined using a FEI Quanta 600 FEG scanning electron microscope (SEM). SEM imaging was conducted at the center of the fusion zone to capture representative microstructural features. Using an accelerating voltage of 10 kV and an acquisition time of 30 µs, images were acquired in secondary electron imaging mode to enhance surface detail contrast.

Vickers microhardness testing was performed on a Buehler hardness tester at a 0.5 N load (HV 0.5), following the ASTM E92-17 standard for hardness measurement (Ref. 44). Each sample was subjected to a total of 18 indents, with a dwell time of 20 s. The indentations were placed in two columns along the center of the weld bead, above the melt pool boundary. They were separated by 0.5 mm, 2.5× the indent size for spacing. The precision of the Vickers hardness tester, specified as ±2% HV by Beuhler, was incorporated into the overall uncertainty calculation for each hardness measurement. To

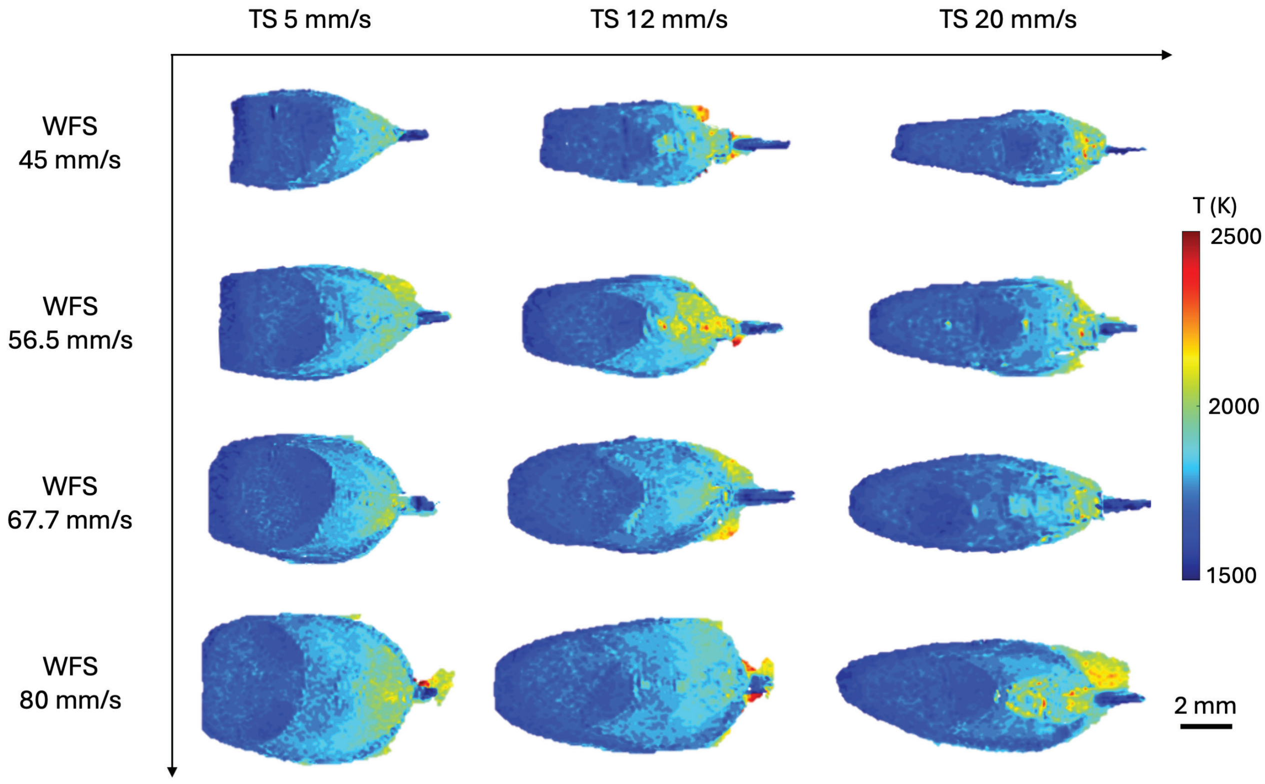

Fig. 7 — Temperature distributions of the melt pool at varying WFS and TS conditions. The rows represent increasing WFS from 45 to 80 mm/s, while the columns correspond to increasing TS from 5 to 20 mm/s. The color bar indicates temperature variations (1500 to 2500 K).

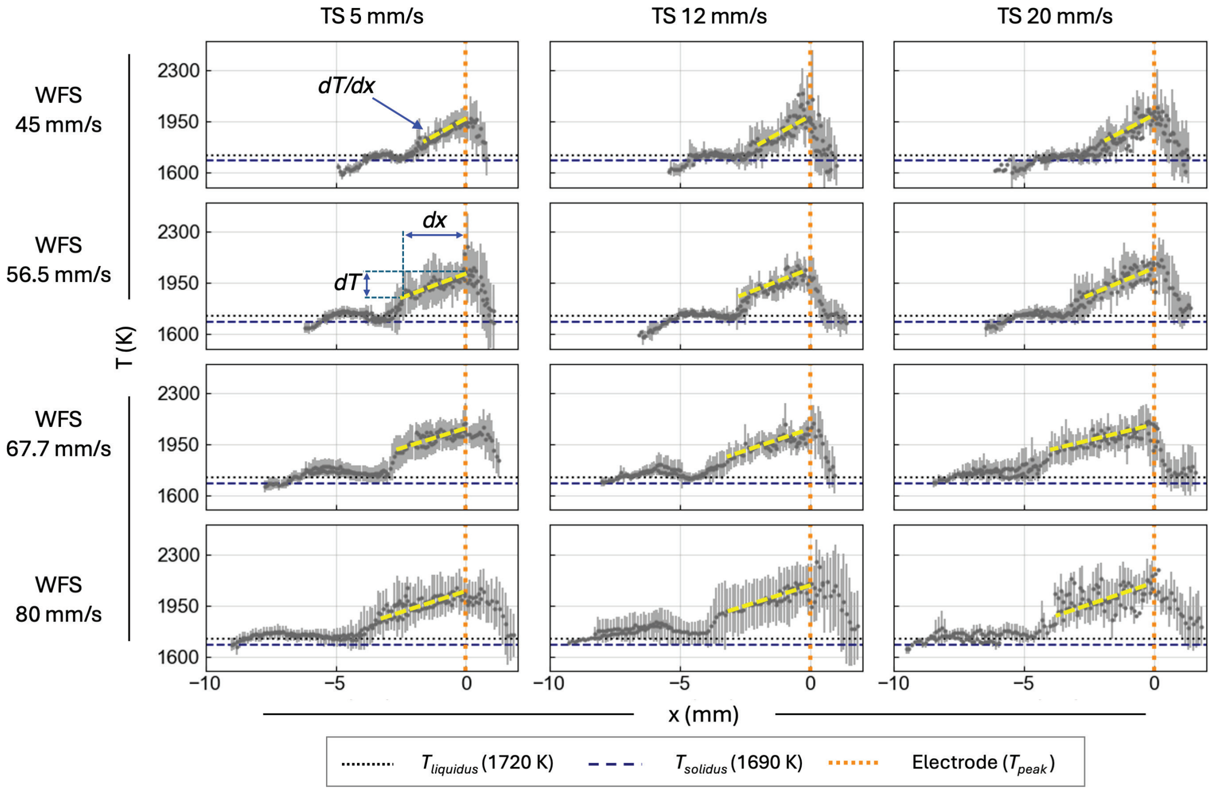

Fig. 8 — Melt pool centerline temperature profiles for varying WFS and TS conditions. Each plot shows the temperature gradient in the range considered for calculating the molten pool cooling rates, the electrode temperature, and the liquidus and solidus temperature intervals.

account for this, we combined the instrument's precision error with the standard deviation from the multiple hardness measurements taken across different sample locations.

Results

The temperature distributions of the melt pool obtained under constant processing parameters of TS = 5 mm/s and WFS = 67.7 mm/s at varying Δt (50, 350, and 1200 μs) are illustrated in Fig. 4. At the shortest Δt of 50 μs, temperatures ranged from 1850–2000 K, highlighting the peak and high-temperature regions near the wire electrode contact point captured during the short-circuiting period. As Δt increased to 350 μs and 1200 μs, lower-temperature distributions became visible, revealing the gradual temperature drop toward the melt pool's tail. The longer Δt captured the cooling regions extending 4–5 mm behind the wire contact point, with temperatures reaching the solidus range (~ 1690 K). Melt pool temperature measurements captured with the two-color technique are shown in Figs. 7 and 8, providing comprehensive insights into melt pool behavior under various processing conditions. Peak temperatures of approximately 2000–2100 K were observed close to the electrode contact point, with gradual temperature reduction toward the tail of the melt pool. Figure 8 shows a map of the temperature profile across the centerline, and Fig. 9A illustrates the measured cooling rates derived from centerline temperature profiles. Cooling rates notably increased with higher TS, reflecting

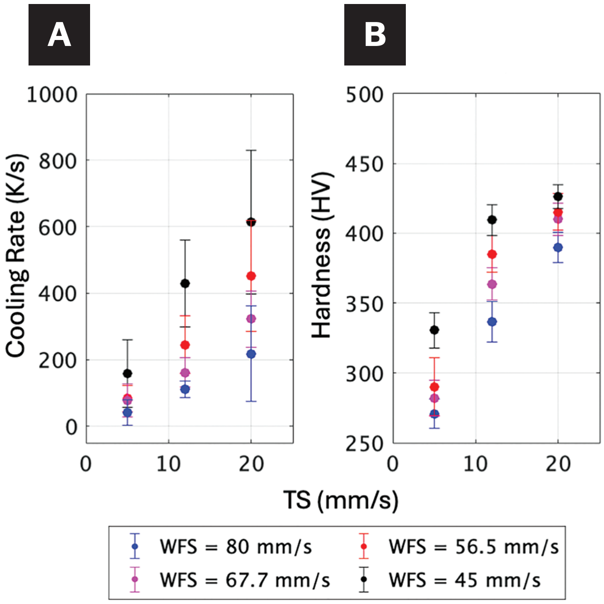

Fig. 9 — A — Molten cooling rates from centerline temperature profiles for varying WFS and TS conditions; B — Vickers hardness measurements from the melt pools corresponding to the same sets of process parameters shown in A, highlighting the influence of WFS and TS on cooling rate and resulting material properties.

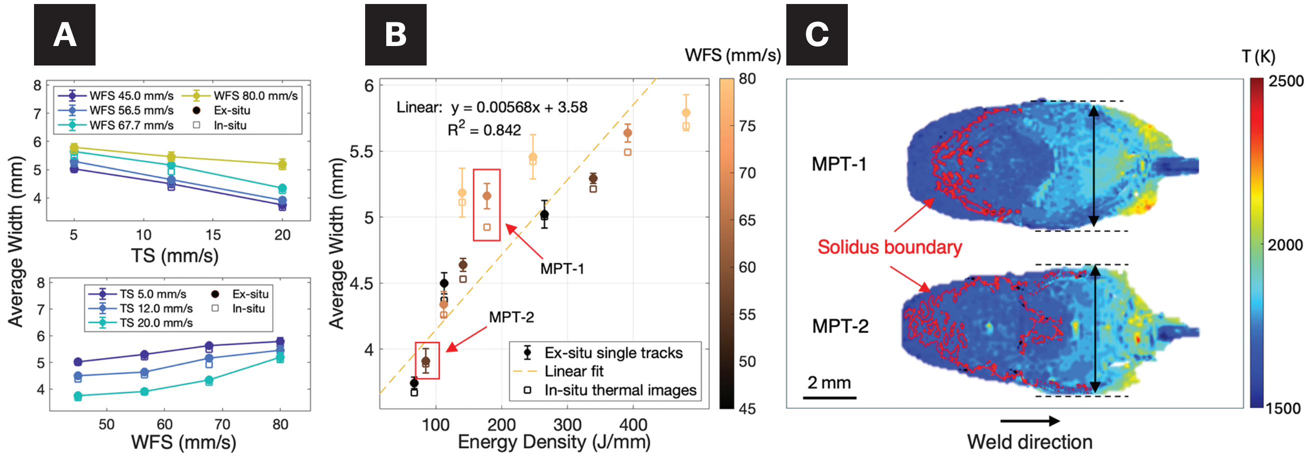

Fig. 10 — A — In-situ and ex-situ melt pool width measurements for varying WFS and TS conditions; B — average melt pool width vs. linear energy density, for ex-situ (error bars show one standard deviation) and in-situ measurements; C — thermal images of MPT-1 and MPT-2 with solidus boundaries (red outline). MPT-1 lacks a visible boundary across the width, indicating only the liquid melt pool, while MPT-2 shows the boundary, resulting in a close alignment with ex-situ measurements.

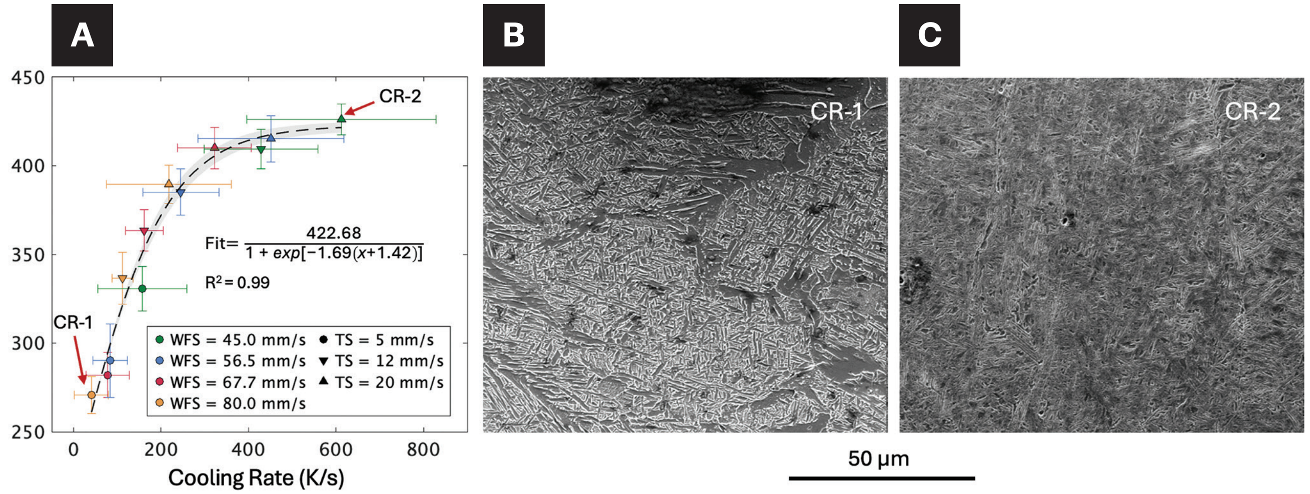

Fig. 11 — A — Observed variation in Vickers hardness and measured molten pool cooling rates, fitted using a fitted logistic function. The bounds on the fitted curve represent the 95% confidence interval, and error bars on experimental data show one standard deviation; B — coarse grain structure from lowest measured cooling rate and hardness, identified as CR-1; C — fine grain structure from highest measured cooling rate and hardness, identified as CR-2.

more rapid heat extraction as the melt pool experienced shorter interaction times with the heat source. Additionally, lower WFS correlated to higher cooling rates, likely due to reduced heat input and melt pool size. These cooling rate variations directly influenced microstructure refinement and subsequent mechanical properties, as discussed in the hardness trends of Fig. 9B.

The relationship between processing parameters and melt pool geometry across multiple WFS and TS measurements provides additional verification of the two-color imaging results. Figure 10A shows the variation of melt pool width with TS and WFS, following expected trends. Figure 10B combines the TS and WFS with the use of linear energy density, defined as the ratio of the average power (calculated from alternating current and voltage, which vary with WFS) and the TS. While melt pool widths from thermal images generally aligned with the ex-situ melt pool width measurements, discrepancies arose depending on the visibility of the solidus boundary in the thermal images. MPT-1 in Fig. 10C shows an example thermal image in which the solidus boundary did not fully extend to the entire melt pool, meaning the in-situ measurement captured only the liquid region and underestimated the full width. The percentage difference between the in-situ and ex-situ width measurements in the case of MPT-1 was less than 5%. In such cases where the solidus boundary was not captured completely, in-situ widths were found to be smaller than ex-situ measurements, as observed in Figs. 10A and B. In contrast, MPT-2 was another scenario where the solidus boundary extended to the maximum width of the melt pool and resulted in an error of less than 1%. In such cases, in-situ width measurements closely matched ex-situ values.

Hardness generally increased with higher TS, likely due to faster cooling promoting finer microstructures. In Fig. 9B, hardness values show a similar trend to the measured cooling rate over the varying TS and WFS combinations. At lower WFS (45 mm/s), the increase in hardness with TS was more prominent, with values rising from around 300 HV at 5 mm/s to over 400 HV at 20 mm/s. The fitted curve in Fig. 11A indicates a strong correlation between molten pool cooling rate and hardness. The hardness slightly plateaued around a measured cooling rate of 400 K/s, suggesting a threshold beyond which further increases in cooling rate resulted in only minimal gains in hardness. These values are consistent with the literature for low-carbon steel processed under similar cooling conditions, where typical hardness values range between 200 and 450 HV, depending on the cooling rate and microstructure development (Ref. 47). The microstructural differences between samples with low cooling rates (CR-1: 56 K/s) and high cooling rates (CR-2: 610 K/s) are evident in the SEM micrographs in Figs. 11B and C, with fast-cooled samples showing significantly finer structures.

Discussion

In-Situ Melt Pool Width Measurements

As demonstrated in Fig. 10, ex-situ and in-situ width measurements generally aligned within errors of less than 5%. These variations were expected to primarily stem from the visibility of the solidus temperature boundary, as seen in both cases in Fig. 10C. For cases with higher width measurement error, such as MPT-1, the solidus boundary did not fully extend to the location of maximum melt pool width, which led to underestimation of the full width when compared to ex-situ measurements. In the case of lower measurement error, such as MPT-2, the solidus boundary extended further toward the front of the melt pool, leading to a better agreement between the in-situ and ex-situ width measurements. These measurements suggest that the two-color method reliably captures melt pool geometry.

Temperature Distributions and Molten Pool Cooling Rates

As expected, when compared to analytical models such as Rosenthal (Ref. 41), it is observed that at each WFS with increasing TS, the melt pool elongated and the width of the high-temperature region reduced. In Figs. 6B and 8, temperature profiles near the liquidus and solidus temperatures exhibited flattening of the curve and a short temperature rise across multiple measurements. This behavior was likely influenced by latent heat release during solidification and rapid solidification-induced undercooling effects. The heat of fusion slowed cooling rates near the phase transition, resulting in a gentler temperature gradient in this region. The consistent temperature patterns across multiple parameter combinations validate the measurement methodology, confirming that temperature distributions represent actual process physics.

The ability to precisely control cooling rates via TS and WFS adjustments is essential for tailoring microstructure and, consequently, mechanical properties in welding and additive manufacturing applications. The systematic variation in thermal gradients observed in Fig. 8 explains the wide range of cooling rates (56–610 K/s) achieved across the processing parameter space. These cooling rates were comparable to those reported in other welding-based processes. For instance, Yang and DebRoy et al. reported simulated cooling rates for double-pulsed GMAW ranging from approximately 10–500 K/s depending on specific welding parameters (Ref. 46). Experimental results for laser-based DED ranged from 100-1000 K/s, driven by variations in laser power and scanning velocity (Ref. 29). In contrast, the cooling rates captured from the laser powder bed fusion process, which involve significantly smaller melt pools (on the order of hundreds of microns), span from 10^3 to 10^6 K/s (Ref. 28). These comparisons illustrate that the cooling rates measured in this study aligned well within the broader context of arc welding and additive manufacturing processes.

Hardness Testing and Microstructure Characterization

Microstructural characteristics, including different phases and sizes (grain size and lath size), are widely recognized as key determinants of mechanical properties. For instance, finer lath structures resulting from higher cooling rates typically yield enhanced hardness due to the refined grain boundaries that impede dislocation movement. The SEM micrographs in Figs. 11B and C illustrate the reduction in lath spacing from the lowest, 56 K/s (CR-1), and highest, 610 K/s (CR-2), molten pool cooling rates measured from real-time thermal images. These observations reinforce the well-established correlation between cooling rate, microstructural refinement, and hardness (Ref. 48).

Challenges in Data Interpretation and Potential Future Work

Extending this technique to different materials and shielding gas environments presents a challenge due to variations in arc emission spectra. The spectral intensity of the welding arc is influenced by shielding gas composition, material type, and process conditions. Since the two-color method using a commercial camera relies on specific spectral bands within the visible range, different filter selections would be required to capture weld pool temperatures (Refs. 49, 50). For example, nickel-based alloys or aluminum-based materials exhibit distinct emission characteristics compared to L-59 steel, requiring different bandpass filters to mitigate arc interference and accurately capture thermal emissions from the weld pool (Ref. 51). The current technique is dependent on the use of SC transfer modes, capturing melt pool temperatures only when the arc is inactive. This presents limitations for processes like spray transfer, where a continuous arc is present. In these cases, a potential solution is to focus temperature measurements on the tail region of the melt pool, where arc interference is relatively lower compared to the area directly beneath the heat source.

While the temperature plots clearly indicate a liquidus-to-solidus transition region (1680–1720 K), attempts to estimate cooling rates within this narrow temperature interval resulted in substantial uncertainties. Therefore, cooling rates were defined over a broader temperature range from the peak temperature (~ 2000 K) down to approximately 1800 K, ensuring improved measurement repeatability and reduced sensitivity to fluctuations. For materials with lower melting temperatures, the solidification interval might fall outside the spectral sensitivity range of the current RGB camera, thus limiting its applicability. Future work could explore integrating an RGB sensor with a longer-wavelength infrared sensor to extend the measurable temperature range, preserving the advantages of real-time thermal imaging.

The existing camera setup, combined with the selected filters and thresholding, resulted in low usage (~ 18%) of the low-power duty cycle. Increasing the camera frame rate to 200 fps could improve data capture efficiency without altering the core setup (see Appendix A.4). Even without such adjustments, the strong correlation observed between in-situ thermal data and hardness demonstrates the effectiveness of the current technique for in-situ melt pool monitoring and mapping hardness variations.

Conclusions

This study advanced thermal monitoring of the welding and welding-based additive manufacturing processes by applying a novel two-color method with a commercial color camera to accurately capture temperature measurements within the melt pool using real time images. This technique was then utilized to establish a direct correlation between measured molten-pool cooling rates from the temperature data and hardness measurements. This correlation demonstrated the predictive quantification of mechanical properties during the manufacturing process, enhancing the precision of non-destructive material property assessments.

Key enhancements to the thermal imaging method included the use of bandpass filters, which effectively reduced arc intensity noise and allowed for accurate thresholding by excluding non-thermal images caused by pixel oversaturation and during the arcing period. This refinement was essential in improving the reliability of temperature measurements by making sure that the measurements acquired were only from the thermal melt pool frames. Additionally, temporal thresholding techniques differentiated high-intensity frames from lower-intensity frames that were more suitable for analysis, thus refining the data used to quantify the temperature-hardness relationship. The findings show that higher cooling rates, commonly associated with increased TS, lead to finer microstructure and, consequently, improved hardness.

This study also provides an experimentally validated approach for measuring melt pool temperatures that can support physics-based models. Many existing models rely on fluid flow simulations without direct validation of temperature fields, which are crucial for understanding defect formation mechanisms such as porosity and cracking. By offering a commercially accessible and economically affordable method for measuring melt pool temperatures, this work can support numerical modeling efforts in addition to making real-time thermal monitoring more feasible for broader adoption in research and industrial applications.

Acknowledgments

This research was sponsored by the Army Research Laboratory, United States, and was accomplished under Cooperative Agreement Number W911NF-20-2-0175, and the Manufacturing Futures Institute at Carnegie Mellon University. Alexander J. Myers and Guadalupe Quirarte are supported by the National Science Foundation Graduate Research Fellowship Program under Grant No. DGE2140739 & DGE1745016. The views and conclusions contained in this document are those of the authors and should not be interpreted as representing the official policies, either expressed or implied, of the Army Research Laboratory, National Science Foundation, or the U.S. Government. The U.S. Government is authorized to reproduce and distribute reprints for government purposes, notwithstanding any copyright notation herein.

Appendix A — Supplementary Information

Appendix A.1 — Metal Transfer Modes in GMAW (STT vs. SC)

The surface tension transfer (STT) mode is characterized by its reactive waveform, designed to minimize spatter and improve weld bead quality by precisely controlling droplet detachment through distinct phases. These phases can be seen in Fig. A.12: (1) background current, (2) pinch current, (3) peak current, and (4) tail-out current. This method uses a feedback loop to instantly adjust current based on arc voltage signals, providing low heat input and stable metal transfer ideal for thin materials and open-root applications. In contrast, conventional short-circuit (SC) relies on the wire feed speed (WFS) to characterize the current and voltage waveforms, exhibiting pronounced voltage drops during metal droplet contact, followed by abrupt voltage peaks upon arc reignition. Unlike STT, SC does not use active voltage sensing or real-time adaptive current control, making STT superior in applications requiring precise heat management and reduced spatter (Ref. 32).

Appendix A.2 — WFS and Power Correlation

Voltage and current profiles were recorded during the welding process at various travel speed (TS) and WFS combinations. The profiles shown in Fig. A.13A illustrate the real-time fluctuations in both voltage and current across the weld length, which are typical during the dynamic melting and deposition process. These fluctuations were captured to calculate the power applied to the system at each experimental condition. Below the plot, the resulting weld bead is shown, visually confirming the stability and quality of the deposition under the recorded processing parameters. The relationship between power and WFS for three different TS values (5 mm/s, 12 mm/s, and 20 mm/s) is demonstrated in Fig. A.13B. Power was calculated as the product of the recorded voltage and current, averaged over the length of the weld bead.

The linear fit ($P_{avg} = 40 \cdot \mathrm{WFS} - 600$) highlights the proportional relationship between WFS and power, with an R^2 value of 0.99, indicating a strong correlation. The inset equations show how power is derived from the physical principles governing the welding process, linking material properties, thermal behavior, and input parameters. This strong agreement between experimental data and the linear model validates the consistency of the system and its applicability for exploring process-property relationships in WAAM.

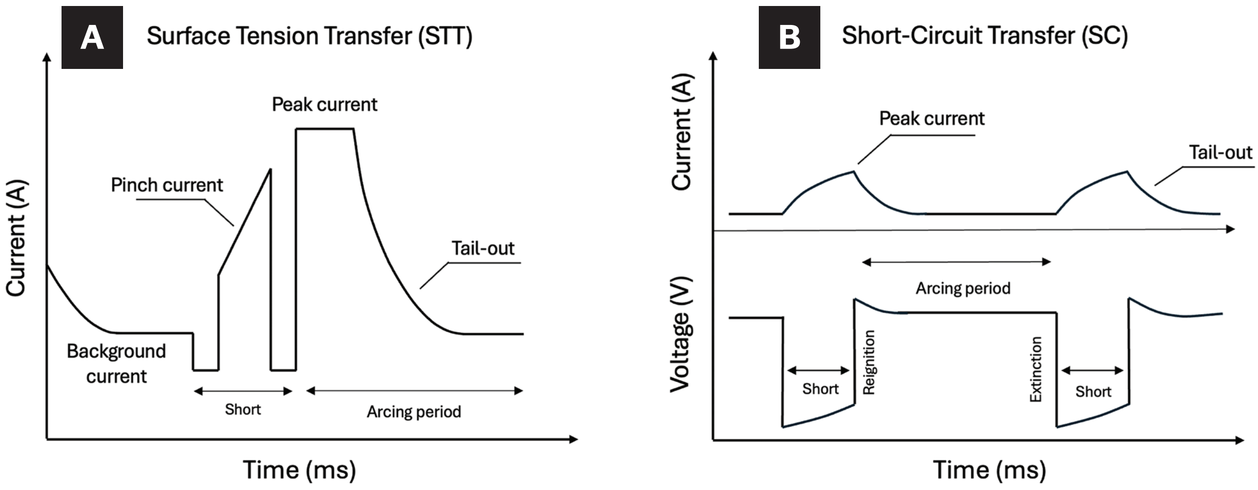

Fig. A.12 — A — STT current waveform; B — SC current and voltage waveform (recreated from Ref. 33).

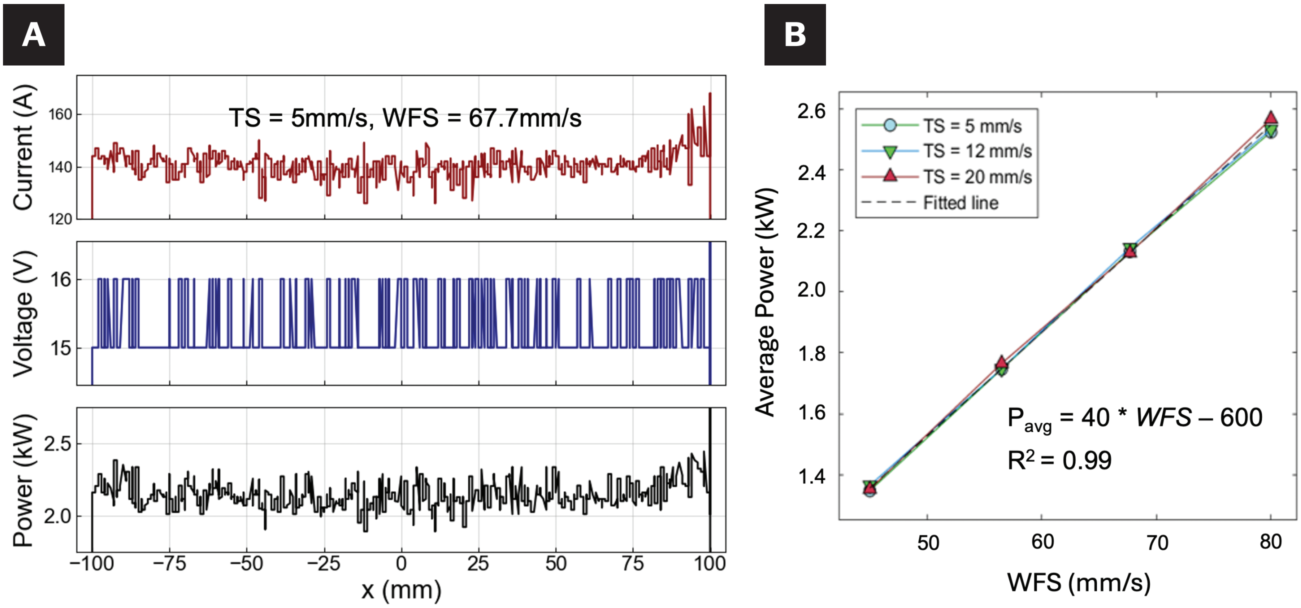

Fig. A.13 — A — Voltage and current profiles recorded during the WAAM process at TS = 5 mm/s and WFS = 67.7 mm/s, and calculated power, all showing real-time fluctuations; B — average Power (P_{avg}) as a function of constant WFS for three TS values (5, 12, and 20 mm/s). The linear fit highlights the linear relationship between WFS and power, with an R^2 value of 0.99.

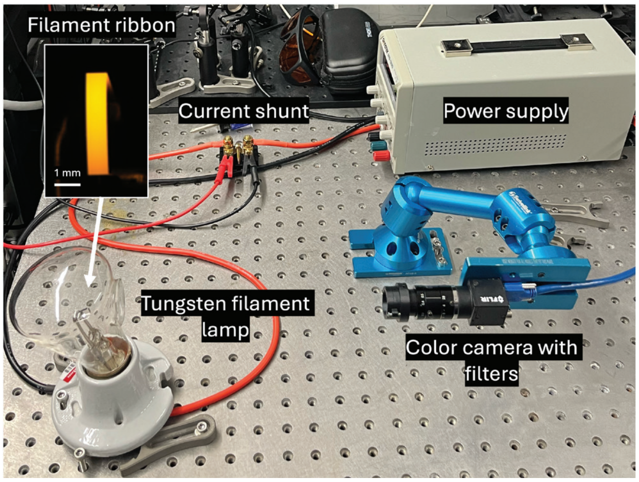

Fig. A.14 — Experimental setup for temperature validation using the NIST calibrated tungsten filament. The Blackfly color camera contains the selected filters for plasma arc interference reduction.

Appendix A.3 — Tungsten Filament Experimental Setup

The experimental setup for the temperature validation can be seen in Fig. A.14.

Appendix A.4 — Image Processing

Homography corrects for perspective distortion, but it does not physically change the camera angle. Figure A.15 shows an example of the homography matrix transformation, including a representation of the melt pool shape to illustrate how it was affected by the transformation. This calibration ensured accurate spatial transformation and allowed us to track pixel dimensions after applying homography.

Figure A.16 illustrates the current waveform recorded during a single-track experiment and the corresponding average pixel intensity. The total duration of deposition was 10.1 s. The system was at low power between the background current and the max pinch current (150-165 A) and occurred for 87.12%

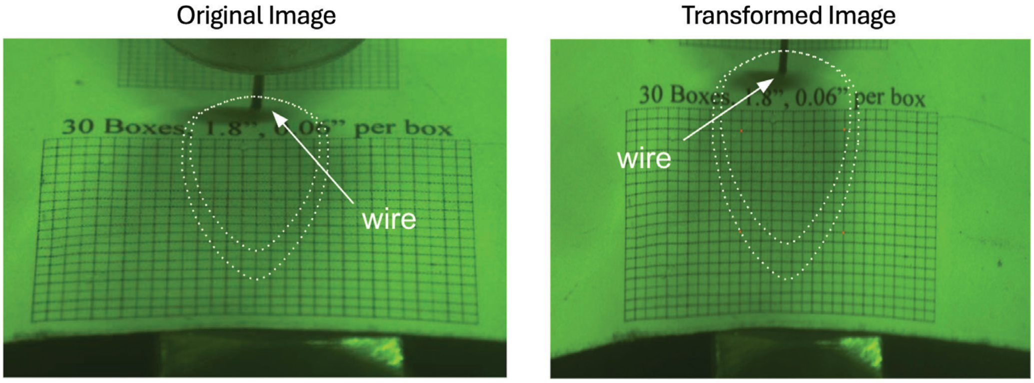

Fig. A.15 — Image on the left shows the region of interest and field of view. The image on the right shows the region of interest as a transformed image after applying homography and correcting for view angle.

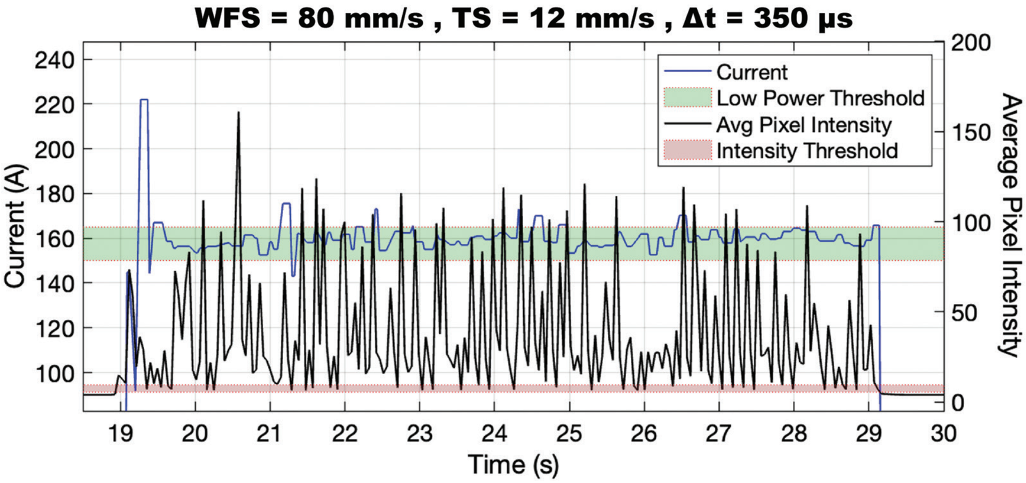

Fig. A.16 — Current waveform recorded during a single-track experiment and the corresponding average pixel intensity in the camera images. Highlighted regions show the threshold in current (power) and pixel intensity used for analysis.

of the total deposition time; 16.67% of the total frames taken during deposition were within the pixel intensity threshold (5.5–9.8). This means that approximately 20% of the low power duty cycle was used for thermal imaging.

$$Duty\ Cycle\ \%\ (Low\ power) = \frac{Number\ of\ data\ points\ in\ low\ power\ cycle}{Total\ number\ of\ data\ points\ during\ deposition} \times 100$$

$$Duty\ Cycle\ \%\ (Low\ power) = 87.12\%$$

$$Duty\ Cycle\ \%\ (Images) = \frac{Number\ of\ frames\ within\ threshold}{Total\ number\ of\ frames\ during\ deposition} \times 100$$

$$Duty\ Cycle\ \%\ (Images) = 16.67\%$$

$$\begin{aligned} &Total\ usage\ of\ low\ power\ duty\ cycle \\ &for\ thermal\ imaging = 16.67/87.12 = 19.13\% \end{aligned}$$

References

1. Angeloni, C., Francioso, M., Liverani, E. Ascari, A., Fortunato, A., and Tomesani, L. 2024. Laser welding in e-mobility: process characterization and monitoring. *Lasers in Manufacturing and Materials Processing* 11(1): 324. DOI: 10.1007/s40516-023-00216-7

2. Kim, Y. S. 2024. Review on welding process monitoring based on deep learning. *Journal of Welding and Joining* 42(4): 1–15.

3. Cai, W., Wang, J., Jiang, P., Cao, L., Mi, G., and Zhou, Q. 2020. Application of sensing techniques and artificial intelligence-based methods to laser welding real-time monitoring: A critical review of recent literature. *Journal of Manufacturing Systems* 57: 1–18. DOI: 10.1016/j.jmsy.2020.07.021

4. Benakis, M., Du, C., Patran, A., and French, R. 2019. Welding process monitoring applications and industry 4.0. *IEEE 15th International Conference on Automation Science and Engineering (CASE)*, p. 1755–1760. DOI: 10.1109/COASE.2019.8843319

5. Zeng, J., Cao, G.-Z., Peng, Y.-P., and Huang, S.-D. 2020. A weld joint type identification method for visual sensor based on image features and SVM. *Sensors* 20(2): 471. DOI: 10.3390/s20020471

6. Zhang, Y. 2008. *Real-time weld process monitoring - An analysis of welding process monitoring and control*. Woodhead.

7. Grasso, M., Remani, A., Dickins, A., Colosimo, B. M., and Leach, R. K. 2021. In-situ measurement and monitoring methods for metal powder bed fusion: An updated review. *Measurement Science and Technology* 32(11): 112001. DOI: 10.1088/1361-6501/ac0b6b

8. Cambon, C., Bendaoud, I., Rouquette, S., and Souli´e, F. 2022. A WAAM benchmark: From process parameters to thermal effects on weld pool shape, microstructure and residual stresses. *Materials Today Communications* 33: 104235. DOI: 10.1016/j.mtcomm.2022.104235

9. Khamari, B. K., Dash, S. S., Karak, S. K., and Biswal, B. B. 2020. Effect of welding parameters on mechanical and microstructural properties of GMAW and SMAW mild steel joints. *Ironmaking & Steelmaking* 47(8): 844–851. DOI: 10.1080/03019233.2019.1623592

10. DebRoy, T., Wei, H. L., Zuback, J., Mukherjee, T., Elmer, J. W., Milewski, J. O., Beese, A. M., Wilson-Heid, A., De, A., and Zhang, W. 2018. Additive manufacturing of metallic components – Process, structure and properties. *Progress in Materials Science* 92: 112–224. DOI: 10.1016/j.pmatsci.2017.10.001

11. Z. X. L. W., and Zhang, K. 2021. Effect of cooling rate on the microstructure and mechanical properties of wire and arc additive manufactured 2319 aluminum alloy. *Materials Science and Engineering* 803.

12. David, S. A., Babu, S. S., and Vitek, J. M. 2003. Welding: Solidification and microstructure. *JOM* 55(6) (2003) 14–20. DOI: 10.1007/s11837-003-0134-7

13. David, S. A., and Vitek, J. M. 1989. Correlation between solidification parameters and weld microstructures. *International Materials Reviews* 34(1): 213–245. DOI: 10.1179/imr.1989.34.1.213

14. Jeong, J., Webster, S., Liao, S., Mogonye, J.-E., Ehmann, K., and Cao, J. 2022. Cooling rate measurement in directed energy deposition using photodiode-based planck thermometry (PDPT). *Additive Manufacturing Letters* 3: 100101. DOI: 10.1016/j.addlet.2022.100101

15. Byers, J., Larsen, M., Webster, S., and Bennett, J. 2024. Assessing melt pool temperature independence from hardness via photodiode-based plank thermometry (PDPT). *Manufacturing Letters* 41: 1109–1115. DOI: 10.1016/j.mfglet.2024.09.136

16. Xie, X., Bennett, J., Saha, S., Lu, Y., Cao, J., Liu, W. K., and Gan, Z. 2021. Mechanistic data-driven prediction of as-built mechanical properties in metal additive manufacturing. *npj Computational Materials* 7(1): 86. DOI: 10.1038/s41524-021-00555-z

17. Xia, C., Pan, Z., Polden, J., Li, H., Xu, Y., Chen, S., and Zhang, Y. 2020. A review on wire arc additive manufacturing: Monitoring, control and a framework of automated system. *Journal of Manufacturing Systems* 57: 31–45. DOI: 10.1016/j.jmsy.2020.08.008

18. Yang, P., Deibler, L. A., Bradley, D. R., Stefan, D. K., and Carroll, J. D. 2018. Microstructure evolution and thermal properties of an additively manufactured, solution treatable AlSi10Mg part. *Journal of Materials Research* 33(23): 4040–4052. DOI: 10.1557/jmr.2018.405

19. Yang, H., Wikle, H., Nagarajan, S., Johnson, M., Banerjee, P., and Chin, B. 2008. "Infrared sensors in welding." In *Real-time weld process monitoring*, 74–103. DOI: 10.1533/9781845694401.1.74

20. Jorge, V. L., Teixeira, F. R., and Scotti, A. 2022. Pyrometrical interlayer temperature measurement in WAAM of thin wall: Strategies, limitations and functionality. *Metals* 12(5): 765. DOI: 10.3390/met12050765

21. Scotti, A. 2019. The potential of IR pyrometry for monitoring interpass temperature in wire + arc additive manufacturing. *Evolutions in Mechanical Engineering* 3(1). DOI: 10.31031/EME.2019.03.000553

22. Hooper, P. A. 2018. Melt pool temperature and cooling rates in laser powder bed fusion. *Additive Manufacturing* 22: 548–559. DOI: 10.1016/j.addma.2018.05.032

23. Richter, A., Gehling, T., Treutler, K., Wesling, V., and Rembe, C. 2021. Real-time measurement of temperature and volume of the weld pool in wire-arc additive manufacturing. *Measurement: Sensors* 17 100060. DOI: 10.1016/j.measen.2021.100060

24. Halisch, C., Radel, T., Tyralla, D., and Seefeld, T. 2021. Online monitoring in WAAM: Using a two colored pyrometric camera for temperature field monitoring in wire arc additive manufacturing. *PhotonicsViews* 18(S1): 2–3. DOI: 10.1002/phvs.202100005

25. Jorge, V. L., Bendaoud, I., Souli´e, F., and Bordreuil, C. 2024. Rear weld pool thermal monitoring in gtaw process using a devel-

oped two-colour pyrometer. *Metals* 14(8): 937. DOI: 10.3390/met14080937

26. Craig, J. Surface and particle imaging pyrometer and method of use. U.S. Patent US5963311A, filed 12 September, 1997, and issued 5 October, 1999. *patents.google.com/patent/US5963311A/fr*

27. Vallabh, C. K. P., Sridar, S., Xiong, W., and Zhao, X. 2022. Predicting melt pool depth and grain length using multiple signatures from in-situ single camera two-wavelength imaging pyrometry for laser powder bed fusion. *Journal of Materials Processing Technology* 308: 117724. DOI: 10.1016/j.jmatprotec.2022.117724

28. Myers, A. J., Quirarte, G., Ogoke, F., Lane, B. M., Uddin, S. Z., Farimani, A. B., Beuth, J. L., and Malen, J. A. 2023. High-resolution melt pool thermal imaging for metals additive manufacturing using the two-color method with a color camera. *Additive Manufacturing* 73: 103663. DOI: 10.1016/j.addma.2023.103663

29. Myers, A. J., Quirarte, G., Beuth, J. L., and Malen, J. A. 2023. Two-color thermal imaging of the melt pool in powder-blown laser-directed energy deposition. *Additive Manufacturing* 78: 103855. DOI: 10.1016/j.addma.2023.103855

30. Bardin, F., Morgan, S., Williams, S., McBride, R., Moore, A. J., Jones, J. D. C., and Hand, D. P. 2005. Process control of laser conduction welding by thermal imaging measurement with a color camera. *Applied Optics* 44(32). DOI: 10.1364/AO.44.006841

31. Lincoln Electric. SuperArc® l-59 GMAW (MIG). Retrieved December 5, 2024, from *lincolnelectric.com/en/Products/superarcl59_gmaw*.

32. Alro Steel. A36 Hot Rolled Pickled and Oiled Steel. Retrieved March 6, 2025, from *alro.com/divsteel/metals_gridpt.aspx?gp=0319&O*.

33. He, F., Yuan, L., Mu, H., Ros, M., Ding, D., Li, H., and Pan, Z. 2024. Fabricating complex parts through optimizing weld bead geometry in WAAM: A comparative study of surface tension transfer and cold metal transfer. *Journal of Manufacturing Processes* 131: 1498–1513. DOI: 10.1016/j.jmapro.2024.09.060

34. Lincoln Electric, Power Wave STT Module, E5.190. June 2020.

35. TWI. MIG/MAG Developments in Low Heat Input Transfer Modes. Retrieved March 6, 2025, from *twi-global.com/technical-knowledge/job-knowledge/mig-mag-developments-in-low-heat-input-transfer-modes-133*.

36. FLIR, BFLY-PGE-23S6C-C: 1.12" Blackfly PoE GigE Color Camera. Retrieved December 5, 2024, from *flir.com*.

37. TamronUSA, M112FM50: 50mm f/2.8 lens for machine vision. Retrieved December 5, 2024, from *tamron-americas.com*.

38. Ancona, A., Sibillano, T., and Lugara, P. M., 2008. Optical plasma spectroscopy as a tool for monitoring laser welding processes. *Journal of Achievements in Materials and Manufacturing Engineering* 31(2).

39. Touloukian, Y. S., and DeWitt, D. P. 2023. *Thermophysical properties of matter*.

40. Mansurov, N. What is aperture in photography? *Photography Life*. Retrieved December 5, 2024, from *photographylife.com*.

41. Tang, M., Pistorius, P. C., Narra, S., and Beuth, J. L. 2016. Rapid solidification: Selective laser Melting of AlSi10Mg. *JOM* 68(3): 960–966. DOI: 10.1007/s11837-015-1763-3

42. Buehler. Automet® 250 Grinder-Polisher. Retrieved December 5, 2024, from *buehler.com/products/grinding-and-polishing/grinder-polishers/automet-250-grinder-polisher-membrane/*.

43. ASTM Committee E04.01. 2023. Standard Practice for Microetching Metals and Alloys. Retrieved December 6, 2024, from store. *astm.org/e0407-23.html.* DOI: 10.1520/E0407-23

44. ASTM Committee E92-17. 2023 Standard Test Methods for Vickers Hardness and Knoop Hardness of Metallic Materials. 2023. Retrieved December 6, 2024, from *store.astm.org/e0092-17.html*. DOI: 10.1520/E0092-17

45. Ghomashchi, R., and Nafisi, S. 2023. Solidification of Al12Si melt pool in laser powder bed fusion. *Journal of Materials Engineering and Performance* 32(23): 10943–10955. DOI: 10.1007/s11665-023-08502-3

46. Yang, Z., and DebRoy, T. 1997. Weld metal microstructure prediction from fundamentals of transport phenomena and phase transformation theory. *Science and Technology of Welding and Joining* 2(2): 53–58. DOI: 10.1179/stw.1997.2.2.53

47. Chakraborty, P., Neogy, S., Sarkar, N. K., Donthula, H., Ghosh, S. K., Nandi, H. K., Gopalakrishna, B., Balasundar, I., and Tewari, R. 2024. Formation of bainite in a low-carbon steel at slow cooling rate – Experimental observations and thermodynamic validation. *Steel Research International*. DOI: 10.1002/srin.202400593

48. Wang, H., Cao, L., Li, Y., Schneider, M., Detemple, E., and Eggeler, G. 2021. Effect of cooling rate on the microstructure and mechanical properties of a low-carbon low-alloyed steel. *Journal of Materials Science* 56(18): 11098–11113. DOI: 10.1007/s10853-021-05974-3

49. Wilhelm, G., Gött, G., Schöpp, H., and Uhrlandt, D. 2010. Study of the welding gas influence on a controlled short-arc GMAW process by optical emission spectroscopy. *Journal of Physics D: Applied Physics* 43(43): 434004. DOI: 10.1088/0022-3727/43/43/434004

50. Murphy, A. B. 2001. Thermal plasmas in gas mixtures. *Journal of Physics D: Applied Physics* 34(20): R151–R173. DOI: 10.1088/0022-3727/34/20/201

51. Jönsson, P. G., Westhoff, R. C., and Szekely, J. 1993. Arc characteristics in gas-metal arc welding of aluminum using argon as the shielding gas. *Journal of Applied Physics* 74(10): 5997–6006. DOI: 10.1063/1.355213

GALA CASSIEL SOLIS, **ALEXANDER J. MYERS**, **GUADALUPE QUIRARTE**, **BARNALI MONDAL**, **JONATHAN A. MALEN** (*jonmalen@andrew.cmu.edu*), and **SNEHA PRABHA NARRA** (*snarra@andrew.cmu.edu*) are with the Mechanical Engineering Dept., Carnegie Mellon University, Pittsburgh, Pa.